CrossMark

Sputtering Behavior of Rough, Polycrystalline Mercury Analogs

H. Biber[1] , J. Brötzner[1], N. Jäggi[2] , P. S. Szabo[1,3], J. Pichler[1], C. Cupak[1], C. Voith[1], B. Cserveny[1], A. Nenning[4], A. Mutzke[5],
M. V. Moro[6], D. Primetzhofer[6], K. Mezger[7], A. Galli[2] , P. Wurz[2] , and F. Aumayr[1]

[1] Institute of Applied Physics, TU Wien, Wiedner Hauptstrasse 8-10, A-1040 Vienna, Austria; biber@iap.tuwien.ac.at, aumayr@iap.tuwien.ac.at
[2] Physics Institute, University of Bern, Sidlerstrasse 5, CH-3012 Bern, Switzerland
[3] Space Sciences Laboratory, University of California, Berkeley, CA 94720, USA
[4] Institute of Chemical Technologies and Analytics, TU Wien, Getreidemarkt 9, A-1060 Vienna, Austria
[5] Max Planck Institute for Plasma Physics, Wendelsteinstraße 1, D-17491 Greifswald, Germany
[6] Department of Physics and Astronomy, Uppsala University, Box 516, SE-752 37 Uppsala, Sweden
[7] Institute of Geological Sciences, University of Bern, Baltzerstrasse 1 + 3, CH-3012 Bern, Switzerland
Received 2022 July 29; revised 2022 October 31; accepted 2022 November 16; published 2022 December 13

Abstract

The solar wind continuously impacts on rocky bodies in space, eroding their surface, thereby contributing significantly to the exosphere formations. The BepiColombo mission to Mercury will investigate the Hermean exosphere, which makes an understanding of the precise formation processes crucial for evaluation of the acquired data. We therefore developed an experimental setup with two microbalances that allows us to compare the sputter behavior of deposited thin solid layers with that of real mineral samples in the form of pressed powder. In addition, this technique is used to study the angular distribution of the sputtered particles. Using 4 keV He^+ and 2 keV Ar^+ ions, the sputter behavior of pellets of the minerals enstatite ($MgSiO_3$) and wollastonite ($CaSiO_3$) is studied, because these minerals represent analogs for the surface of the planet Mercury or the Moon. Pellets of powdered enstatite show significantly lower sputter yields than thin amorphous enstatite films prepared by pulsed laser deposition. 3D simulations of sputtering based on surface topography data from atomic force microscopy show that the observed reduction can be explained by the much rougher pellet surface alone. We therefore conclude that sputter yields from amorphous thin films can be applied to surfaces of celestial bodies exposed to ion irradiation, provided the effects of surface roughness, as encountered in realistic materials in space, are adequately accounted for. This also implies that taking surface roughness into account is important for modeling of the interaction of the solar wind with the surface of Mercury.

Unified Astronomy Thesaurus concepts: Mercury (planet) (1024); Solar wind (1534); Exosphere (499); Laboratory astrophysics (2004)

1. Introduction

The impact of charged particles from the solar wind on rocky bodies like Mercury significantly contributes to their weathering. When no protective atmosphere is present, energetic ions can interact with the planetary surface in an unhindered manner. This interaction modifies mineral grains, leading to spectral reddening (Hapke 2001), amorphization (Loeffler et al. 2009), and might even be a necessary step for the liberation of water from hydrous silicates (Zhu et al. 2019). Another consequence of the impinging solar wind is the ejection of particles from the planet's surface. This process is called sputtering and leads to the emission of particles with typically energies of several eV (Betz & Wien 1994). Only particles with velocities exceeding the escape velocity can overcome the planet's gravitational field, which causes a varying fraction of lost material depending on the mass of the particles. Furthermore, sputtering is a driver of exosphere formation, with ejected material returning to the surface in ballistic trajectories, unless it is ionized (Wurz et al. 2010, 2022). These sputtered particles originate from the top few nanometers, which makes the composition of the exosphere also very sensitive to the planets surface. The BepiColombo Mission is therefore equipped with spectrometers to analyze the exosphere composition, which will also bring further insight into the interaction of Mercury's surface with the solar wind (Benkhoff et al. 2010). Due to the broad variety of materials and ion species, simulations of the sputter contribution to the exosphere formation are needed and only limited studies in the laboratory are possible. However, these are crucial as the commonly used binary collision approximation (BCA) simulations often require adaptation of input parameters (Schaible et al. 2017; Szabo et al. 2020a) or have been shown to be inadequate —like the TRIM code in the SRIM package (Szabo et al. 2018). Until now, both BCA codes and sputter experiments have mostly dealt with amorphous samples rather than realistic (poly-)crystalline samples, due to experimental and computational reasons. Most recently, Morrissey et al. started to utilize molecular dynamics (MD) simulations to investigate the interaction of solar wind with crystalline phases, but also extracted parameters for BCA rather than directly studying the sputter process (Morrissey et al. 2022). Related experiments (Szabo et al. 2018, 2020a, 2020b) so far have focused on amorphous thin film samples because of the use of the quartz crystal microbalance (QCM) technique: this tool allows for very precise measurements of mass changes in situ, but is limited to thin films deposited on the quartz resonators (Hayderer et al. 1999). During thin film deposition, the crystal structure of the sample is usually lost due to the pulsed laser deposition method. To also explore sputter data of crystalline samples, different approaches for sputter yield evaluation are necessary. Previous work by Jäggi et al. (2021) showed first results on measuring sputtering of the pyroxenoid wollastonite ($CaSiO_3$) by 2 keV

Ar$^+$ ions using a QCM that analyzed the mass increase due to sputtered particles sticking on a quartz resonator positioned opposite of the sample (Berger et al. 2017).

The movement of this so-called "catcher" QCM was limited to linear motions, making evaluation and interpretation of the results challenging Berger et al. (2017). Meanwhile, we have modified this setup to allow for direct probing of the distribution of sputtered material in a wide angular range around the irradiated sample and present here a detailed comparison between the total sputter yield and the emission characteristics of sputtered particles for polycrystalline versus amorphous samples. Using 4 keV He$^+$ in addition to 2 keV Ar$^+$ ions we also discuss a case highly relevant for space weathering by the solar wind, as the contribution to solar wind sputtering of He ions is expected to be in the same order of magnitude as for protons (Szabo et al. 2020a).

2. Methods

2.1. Experimental Setup

Impingement of energetic particles onto surfaces leads to a release of material by the sputtering of surface atoms. The mass change per area Δm due to sputtering depends on the total ion flux Φ impinging on the sample, the irradiation time t and the sputter yield Y, i.e., the number of particles released per incident ion and the particle mass m_p: $\Delta m = m_p \times Y \times \Phi \times t$. When investigating dynamic changes of the sputter behavior, the sensitivity to these mass changes is often a limiting factor. The QCM technique is a very delicate tool for this task and allows to resolve mass changes corresponding to the submonolayer regime (Hayderer et al. 1999). To utilize this technique in its original form, the sample material has to be deposited as a thin film onto a quartz resonator. For mineral samples, e.g., pulsed laser deposition (PLD) turned out to be ideal for sample preparation (Hijazi et al. 2017; Biber et al. 2020; Szabo et al. 2020a), as the mineral stoichiometry can be preserved in the deposition process. However, in contrast to the original minerals, the resulting films are amorphous. Annealing processes, which could lead to crystallization of the films, are hindered by a destructive phase transition of the used quartz resonators at 847 K (Coe & Paterson 1969; Stadlmayr et al. 2020a). As experiments have recently demonstrated differences in the sputter behavior between amorphous and polycrystalline tungsten (Schlueter et al. 2020), it cannot be assumed a priori that these vitreous films represent the source material well. Furthermore, investigating the impact of surface roughness on the sputtering of mineral samples is also very difficult this way, as these films typically do not show a significant roughness. Therefore, we could not make straightforward use of our traditional TU Wien QCM technique for sputter experiments, where the quartz resonator itself is irradiated with ions. In our upgrade of the setup, we place another resonator in the direct vicinity of an irradiated sample to analyze the mass increase due to sputtered atoms deposited there, rather than the mass loss on the irradiated sample. This allows us to overcome the limitations that conventional film deposition techniques place on the QCM method, such that almost arbitrary bulk samples can be investigated. By moving the catching QCM (catcher) in a circular arc around the sample, additionally the angular distribution of the ejected material can be probed. This method has already shown its capabilities in different experiments with metal samples (Berger et al. 2017; Stadlmayr et al. 2020b;
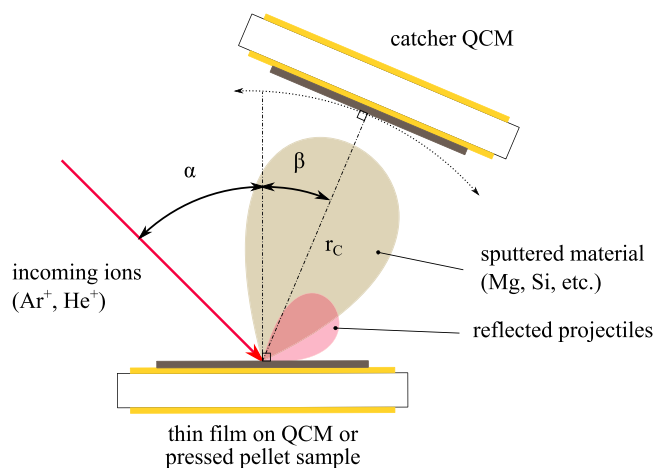

Figure 1. Experimental geometry: incoming projectile ions are hitting the thin film sample on the QCM or a pressed mineral pellet under an impact angle α with respect to the surface normal. Sputtered particles are registered as a mass increase on the "catcher" QCM positioned under an angle of β with respect to the surface normal at a distance $r_C = 17$ mm from the center of the sample.

Cupak et al. 2021). In these cases, the irradiated samples and the coating on the catcher were exactly the same material. This represents an ideal case, as no changes in stoichiometry of the catcher during deposition are expected. For sputtering of compounds like the minerals used in this study, a dynamic variation in sticking probability is possible, leading to transient effects in the measurements. First results with such a catcher were already presented in Jäggi et al. (2021), where deposition rates at different geometries during irradiation of the mineral wollastonite (CaSiO$_3$) with 2 keV Ar$^+$ ions were probed.

In contrast to the previous studies, the setup was drastically modified as depicted in Figure 1 to allow for a direct sweep of the angle β between the catcher and the sample's surface normal via a second manipulator for the catcher. This second manipulator is linked coaxially with the primary holder, thus locking the movement in the plane normal to the manipulator axis. The catcher is placed at a distance of $r_C = 17$ mm to the axis, facing inward. Its surface normal is therefore always pointing to the center of the irradiated sample, which is placed on the axis of rotation. Considering a sensitive area of the catcher quartz resonator with a diameter of 7 mm, this results in a detector solid angle of 0.13 sr. Note that experimental signals from the catcher QCM result from an average over this area weighted with a Gaussian sensitivity function (see Berger et al. 2017 and references therein). The coaxial positioning of the irradiation center and the catcher allows to probe the angular distribution of sputtered particles at a fixed distance. The value range of β is limited in backward direction due to a blocking of the incoming ion beam by the catcher. In forward direction, there is no physical limitation, but large angles of β are undesirable as no particles are deposited anymore. These points therefore do not contribute to any gain of knowledge while the samples still have to be irradiated and are therefore eroded during the measurement.

Two types of samples are installed for irradiation on top of each other on the primary sample holder. One compartment is equipped with a pressed mineral pellet (referred to as pellet), produced in Bern as described in Section 2.2 and Jäggi et al. (2021). The mineral powder pressed into stainless steel holders acts as a polycrystalline mineral sample. In the second compartment, a corresponding thin film on a QCM is mounted

(thin film sample). The stoichiometry of the used thin films was inspected via time-of-flight elastic recoil detection analysis (ToF-ERDA) measurements, guaranteeing comparability between both types of samples (details can be found in Section 2.2). The use of the thin film allows for direct investigation of the total sputter yield of amorphous samples with a given stoichiometry (Hijazi et al. 2017; Szabo et al. 2018, 2020a). By using the catcher QCM, we can make a first order approximation of the pellet sputter yield: We determine a scaling factor r by computing the total signal ratio at the catcher for both sample materials. Scaling of the sputter yield of the thin film on a QCM Y_{QCM} with r then gives an approximation of the total pellet sputter yield:

$$Y_{pellet} = r \times Y_{QCM}. \qquad (1)$$

This approximation is valid under the assumption that both QCM and pellet have the same angular distribution of sputtered particles. However, as we discuss later, this is not the case for rough pellet surfaces, which makes a more extensive measurement of the angular distribution necessary for calculating r and subsequently the sputter yield. Both sample types are irradiated one after the other which allows for direct comparison between the signals at the catcher under otherwise identical conditions.

The ion beam setup is described in detail in Szabo et al. (2018). It allows to use singly or multiply charged ions with a m/q separation achieved via a magnetic sector field (Galutschek et al. 2007). In addition, a set of computer controlled deflection plates was added in front of the first aperture. These are used for switching the ion beam on/off electronically without moving parts, which might interfere with the sensitive QCM signals. Furthermore, a Prevac FS40 A1 electron flood source was installed, facing the sample holder. It is capable of delivering up to 100 μA low energy electrons ($<20\,eV$), which is sufficient to prevent charging of the insulating pellets due to the impinging ion beam.

2.2. Sample Preparation and Measurement Procedure

The production of the pressed mineral pellets and their chemical analysis are described in detail in Jäggi et al. (2021). In short, the pellets were produced by pressing of about 0.01 g of mortared material with grain sizes smaller than 100 μm into the stainless steel holders by applying 80 MPa (at a pellet diameter of 10 mm). To enhance adhesion, a base layer of about 0.02 g wollastonite was added below, which has been found to increase pellet stability. This layer is completely covered by the desired material (either wollastonite or enstatite) and does therefore not alter the irradiation results. For the thin film deposition PLD was used, as discussed in Szabo et al. (2018). Both the wollastonite and enstatite sample were ablated with a KrF excimer laser (Lambda Koherent Pro), which produces 248 nm pulses with 400 mJ (approx. 120 mJ and 1.5 J cm^{-2} at the sample) at 5 Hz. The Au-covered quartz resonator substrates were placed at a distance of 6 cm, and heated to 300 °C. The deposition was performed with an O_2 background pressure of 0.04 mbar for 60 minutes. In the case of wollastonite, a single mineral piece could be utilized as donor, whereas no enstatite fragments of sufficient size were available. Therefore, several pellets were produced from one enstatite sample to be used for both ion beam irradiation and thin film production via PLD, respectively. The stoichiometries of the deposited films were analyzed by means of ToF-ERDA with a 36 MeV I^{8+} ion beam (Moro et al. 2019), and were found to match the original composition of the minerals very well. The composition of the

pressed mineral pellets can be found in Jäggi et al. (2021), whereas thin film compositions are presented in Szabo et al. (2020a) (wollastonite) and listed in Table 5 in the Appendix (enstatite). Inspection with polarized light as well as X-ray diffraction showed that films produced by PLD are amorphous (Szabo et al. 2018, 2020b). This makes their results immediately comparable to commonly used BCA simulations like TRIM (Biersack & Haggmark 1980) or SDTrimSP (Mutzke et al. 2019), where amorphous solids are assumed.

The primary quartzes were prepared for measurements by sputter cleaning with 2 keV Ar^+ ions under an angle of incidence of $\alpha = 60°$ to remove any surface adsorbates due to sample storage on air. By measuring the resonance frequency during these irradiations, the cleaning progress could be monitored and stopped when a steady sputter yield was reached. The same fluences were also used for cleaning the pellet, where no direct feedback signal was available. This means, however, that all samples suffered from ion-induced damaging in the first few nanometers, amorphizing the crystalline phases in the near surface region. This could be of concern for the experiments with He ions, but the fluences applied during one angular sweep of β were in the range of 10^{21} ions $\times$ m^{-2}. For that fluence, the layer initially damaged due to the cleaning process gets removed already in the beginning and damages due to He dominate, as was observed for olivine (Carrez et al. 2002) and estimated for an magnesium and iron rich pyroxene in Biber et al. (2020). For experiments with Ar ions, the surface amorphization due to cleaning is of no concern, as the sputter yield is an order of magnitude higher. Due to this high sputter yield in combination with a penetration depth of only 1.1 nm (according to SDTrimSP), a steady state of damage production and sputtering is easily reached during the measurements.

For the preparation of the catcher, different approaches were used, to test the robustness of the experimental method. In the cases of wollastonite, a quartz resonator coated with a thin wollastonite film was used as catcher. The surface was cleaned with 2 keV Ar^+ ions under normal incidence ($\alpha = 0°$), until steady state sputter yields from wollastonite were obtained. The actual measurements were then directly started with the clean wollastonite surface. This procedure resulted in slight variations of the catcher signals for different days of irradiations, which is attributed to slight changes in initial sticking probabilities. However, the total signal ratios r obtained between pellet- and QCM irradiation remained unaffected for different measurement days. As only this ratio is needed for calculating Y_{Pellet} using Equation (1), this allowed for a quantitative evaluation of pellet sputter yields. For the enstatite, an additional sequence was introduced. Thereby, the pellet was irradiated for a prolonged time, with the catcher at $\beta = 25°$, where significant deposition of material was expected. This was carried out, until a constant signal was obtained, which means that a steady state surface concentration and a constant sticking probability were reached. Under these conditions, sequences with different orders of irradiation were carried out, all resulting in the same, reproducible total signals.

During the measurements with the catcher, the ion beam was scanned with a square profile of 16 mm^2 across the sample. Before and after each irradiation sequence, the ion flux as well as the total impinging ion current were determined with a Faraday cup. Both quantities are important, as the fluence ([ions $\times$ m^{-2}]) is needed to quantify ion-induced effects on the samples, while the total ion current determines the signal at the
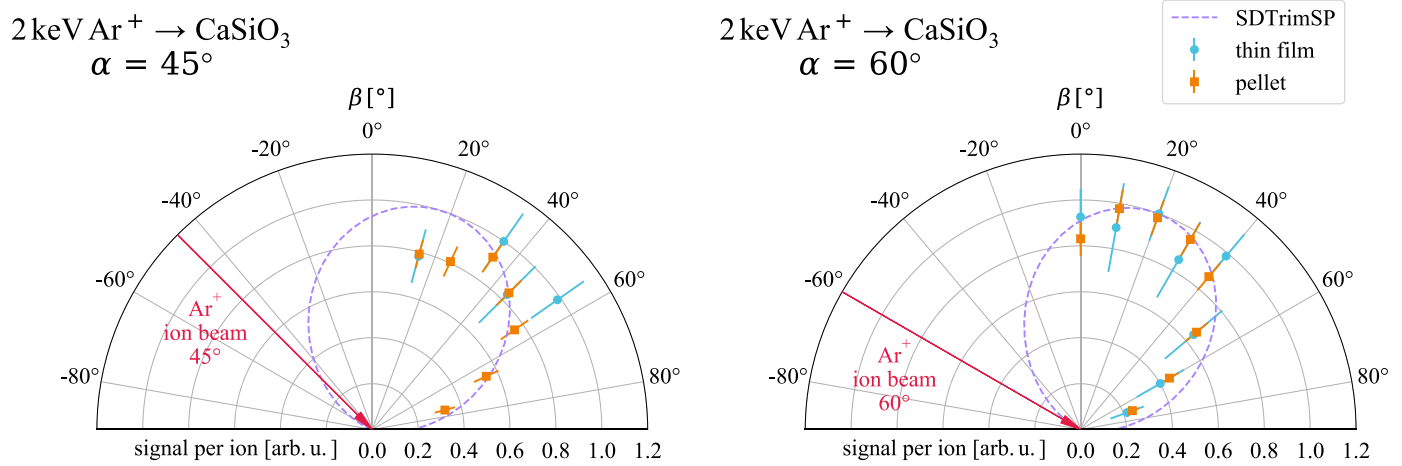
Figure 2. Comparison between the angular dependence of the sputtered particles for irradiation of the wollastonite pellet (orange squares) and the amorphous thin wollastonite film on a QCM (blue circles) with 2 keV Ar^+ ions. Two different angles of ion incidence were probed: $\alpha = 45°$ (left) and $\alpha = 60°$ (right). A fit of the shape $A\cos(\beta - \zeta)^n$ to SDTrimSP results for trajectories in the same angle as the sensitive catcher area is shown as purple line.
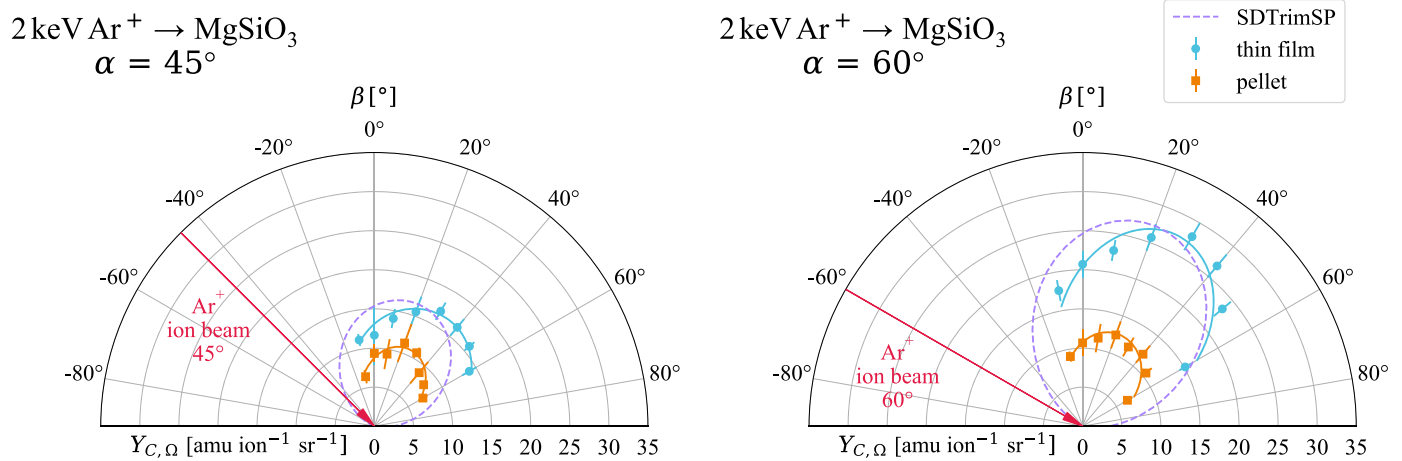

Figure 3. Comparison between the angular dependence of the sputtered particles for irradiation of the enstatite pellet (orange squares) and the enstatite thin film (blue circles) with 2 keV Ar^+ ions. Two angles of ion incidence were probed: $\alpha = 45°$ (left) and $\alpha = 60°$ (right). A fit of the shape $A\cos(\beta - \zeta)^n$ to the experimental data and to SDTrimSP results for trajectories in the same angle as the sensitive catcher area is shown as purple line.

catcher. With the known geometry, the mass change per ion and solid angle $Y_{C,\Omega}$ can be calculated from Sauerbrey's Equation (Sauerbrey 1959), similarly as done in Golczewski et al. (2009), and as outlined in detail in the Appendix.

3. Experimental Results

3.1. Angular Distribution of Sputtered Material

Experiments with different ion species, angles of incidence and analog samples were carried out to gain a broader understanding of data obtained with the catcher technique. For all cases, the angle β between the sample surface normal and the catcher was changed incrementally.

The wollastonite samples represent an ideal test case for studying the setup and the method. Sputtering of thin wollastonite films has been investigated widely in laboratory experiments by Szabo et al. (2018, 2020a) and can be reproduced with SDTrimSP. It is not a typical analog for Mercury, but acts as a FeO-free end member mineral, relevant due to the low expected Fe content on Mercury's surface (Jäggi et al. 2021). For this mineral, the investigations were limited to Ar irradiations. Figure 2 shows the signals of the catcher in the

wollastonite case for the two different Ar^+ impact angles $\alpha = 45°$ (left) and $\alpha = 60°$ (right). The angle β is given with respect to the sample surface normal (see Figure 1), positive β angles denote sputtered particle ejection in forward direction. Therefore, ion beams indicated by the red arrows are coming from negative angles, i.e., from the left side in Figure 2. Both plots in Figure 2 directly compare signals obtained when irradiating the thin film (blue circles) and the pellet (orange squares). At $\alpha = 60°$ the data points show excellent agreement between pellet and thin film. For $\alpha = 45°$, two of the four data points match perfectly and only one outlier, not matching up within the estimated experimental error, is present. Overall, the measurement data of pellet and thin film match very well, i.e., same size and angular dependence. The signals for large values of β ($>50°$) are decreasing faster for $\alpha = 60°$ impact compared with $\alpha = 45°$, which means a lower deposition rate near the surface plane at more gracing ion incidence.

A comprehensive study has been carried out for enstatite, as it serves as analog material for the planet Mercury, which has a Mg content of about 16 wt% in magnesium rich terrains (McCoy et al. 2018; Jäggi et al. 2021). In Figure 3, data for irradiations with 2 keV Ar^+ ions under the angles $\alpha = 45°$ and $60°$ are
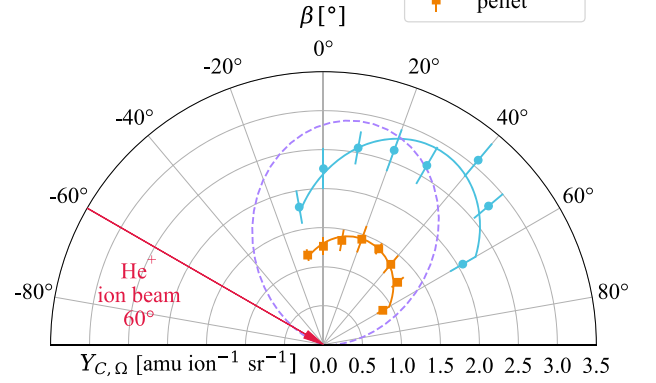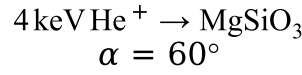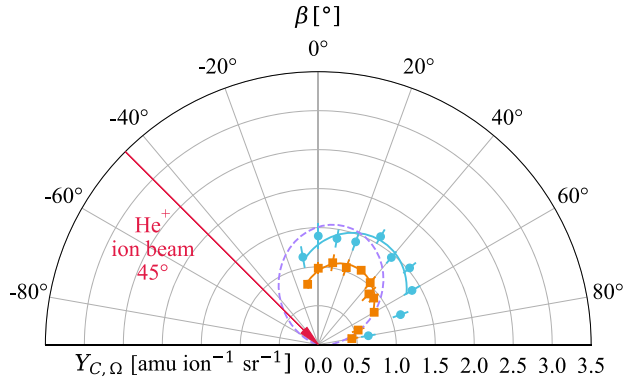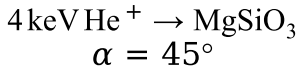
Figure 4. Comparison between the angular dependence of the sputtered particles for irradiation of the enstatite pellet (orange squares) and the enstatite thin film (blue circles) with 4 keV He$^+$ ions. Two angles of ion incidence were probed: $\alpha = 45°$ (left) and $\alpha = 60°$ (right). A fit of the shape $A \cos (\beta - \zeta)^n$ to the experimental data and to SDTrimSP results for trajectories in the same angle as the sensitive catcher area is shown as purple line.

shown, directly comparing both pellet and thin film sample. Due to the prolonged coating of the catcher before the actual measurements, absolute values are robust and $Y_{C,\Omega}$ in amu/ion × sr could be calculated. A fit of the shape $A \cos (\beta - \zeta)^n$ with the free parameters A, ζ and n was added to the data. The pellet/thin film ratio r was later calculated from the integrals of these fits. The same procedure was applied to measurements performed with enstatite samples and the solar wind relevant He$^+$ ions at an energy of 4 keV (Figure 4). Both series show a similar trend. Signals for pellets are significantly lower than when irradiating the thin film samples, with an even bigger difference noticeable at an angle of incidence of $\alpha = 60°$.

3.2. Thin Film Sputter Yield

For the determination of total pellet sputter yields from experimental data only, reference sputter yields from thin films are necessary. The sputter yields directly obtained for thin films on resonators are listed in Table 1, including data from Szabo et al. (2020a) for wollastonite, which was verified during this study. Furthermore, the data obtained for enstatite are shown as squares in Figure 5. The sputter yields obtained for thin films serve as calibration standard for the catcher as discussed in Section 2.1.

4. Discussion and Modeling

For the irradiations of wollastonite, signals obtained at the catcher for both, the thin film and pellet samples, match very well. With the excellent agreement of the data points in this case, a simple evaluation by integration via summing of values with shared β of pellet and thin film is performed (Equation (A5) in the appendix). The ratios r are 0.92 for $\alpha = 45°$ and 1.0 for $\alpha = 60°$ and resulting sputter yields according to Equation (1) are listed in Table 2. Regarding the distributions of sputtered particles, one would expect an emission cone that is more shifted toward the forward direction for higher impact angles, if any dependence of ζ on α is present at all. However, the opposite is observed and catcher signals for increasing angles of β (>50°) are dropping faster for $\alpha = 60°$ than $\alpha = 45°$. This discrepancy might be related to the particular experimental method, measuring the net-deposition rates at a quartz resonator. Ions reflected from the sample will also hit the catcher, where they cause sputtering of material and

Table 1
Sputter Yields Y_{QCM} as Obtained from the Thin Film (QCM) for the Used Combinations of Ions and Irradiated Samples

	Thin Film Sputter Yields [amu/ion]		
	Wollastonite	Enstatite	
α	Ar	Ar	He
0°	21.0 ± 1.5	17.6 ± 2.1	1.8 ± 0.14
30°	36.3 ± 3.8	55.0 ± 11.0	…
45°	58.2 ± 5.5	78.3 ± 9.4	4.8 ± 0.42
60°	89.8 ± 6.6	132 ± 15.9	9.5 ± 0.82

Note. The wollastonite data are from Szabo et al. (2020a) and were verified during this study.

therefore a reduction of deposition rates. This is more likely to occur for $\alpha = 60°$ and at angles close to $\beta=\alpha$. According to SDTrimSP simulations, the reflection coefficients are 4.2% for $\alpha = 45°$ and 14.3% for $\alpha = 60°$. Figure 8 in the Appendix shows the distribution of reflected ions into the catcher solid angle. It can be seen clearly that the ions are scattered directly into the direction where signals at the catcher are smaller than expected for $\alpha = 60°$, where the reflection coefficient is higher by more than a factor of three.

Nevertheless, we conclude from the obtained distributions, that in the case of 2 keV Ar$^+$ irradiations of wollastonite, thin films on quartz resonators are a well suited substitute for realistic wollastonite minerals as far as sputtering is concerned.

For enstatite, however, a different picture emerges at the first glance. When irradiating the pellet, the total signals are significantly reduced compared with the thin film. This is also reflected in the ratio r, this time calculated from the integrals of the cosine fit functions, and the sputter yields which are also listed in Table 2 and shown in Figure 5 (circles). Furthermore, the angular distributions of sputtered material from the pellet shown in Figures 3 and 4 are not only smaller, but also shifted more toward the surface normal ($\beta = 0°$) with the fit parameter for the tilt angle ζ ranging from 21° to 25° for the pellet and 27°–34° for the thin film.

Surface roughness is known to have a significant effect on the sputter yield of materials (Küstner et al. 1998; Küstner et al. 1999; Arredondo et al. 2019); Cupak et al. 2021) and references therein). Cupak et al. have shown in a recent
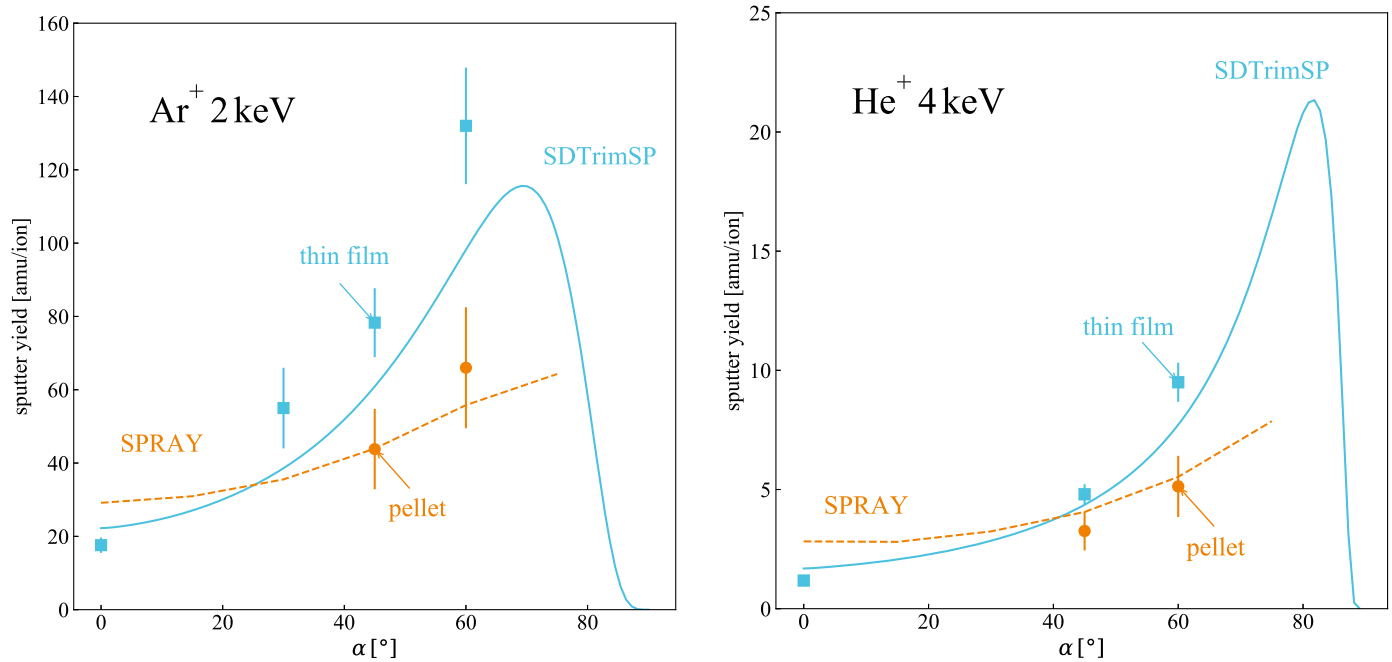
Figure 5. Angular dependence of the sputter yield of enstatite for 2 keV Ar^+ (left) and 4 keV He^+ (right). Data are shown for SDTrimSP (full lines), the pellet (according to Equation (1), circles), the thin film (squares) and SPRAY (dashed lines). The fit to the SDTrimSP data was obtained using the fit formula according to Eckstein & Preuss (2003).

Table 2
Sputter Yields Y_{PELLET} Calculated from the Thin Film Sputter Yields Y_{QCM} and the Ratios r between Catcher Signals of Thin Film and Pressed Mineral Pellets. The Corresponding Values of r are Shown as Well

		Pellet Sputter Yields [$^{amu}/_{ion}$]		
	α	Wollastonite	Enstatite	
		Ar	Ar	He
Y_{Pellet}	45°	53.5 ± 13.3	43.8 ± 11.0	3.26 ± 0.82
	60°	89.8 ± 22.5	66.0 ± 16.5	5.13 ± 1.28
r	45°	0.92 ± 0.18	0.56 ± 0.13	0.68 ± 0.14
	60°	1.0 ± 0.20	0.50 ± 0.10	0.54 ± 0.11

publication that atomic force microscopy (AFM) probes the surface at a suitable scale to characterize roughness for ion beams (Cupak et al. 2021). Based on experiments and simulations, it was also concluded, that the mean surface inclination angle δ_m obtained from AFM images is a good parameter to quantify the effect of sample roughness on sputtering. A theoretical approach including the effects of sputtering on local slopes, shadowing and redeposition by Szabo et al. (2022a) supports this finding. We therefore also used an AFM to characterize our samples. Figure 6 shows AFM images of a thin enstatite film on a QCM (6(a)) and of a pressed enstatite pellet (6(b)) before irradiation. The distributions of the surface inclination angles for representative images are shown in Figure 7. Table 3 lists the average δ_m for all used types of samples, obtained from sets of AFM images. For the thin films of both materials, only minor deviations from perfectly flat samples are expected, as was already observed in previous studies and also noted by Cupak et al. (2021). The wollastonite pellet shows a similar small value of $\delta_m = 17.1°$ as the thin PLD film ($\delta_m = 13.4°$), indicating that roughness effects only play a minor role there as well. For the enstatite pellet however, a significantly higher roughness is observed

with $\delta_m = 35.7°$. Also, the surface inclination angle distribution has a very different shape (see Figure 7). Surface roughness is therefore expected to have a significant impact on the sputter behavior for this sample. For each material, always the same pellet sample was used.

To quantify the effects of surface roughness on the experimental results, computational investigations were used. First, the sputter yields of flat samples were calculated with the BCA code SDTrimSP version 6.03 (Mutzke et al. 2019). Such calculations are only representative for flat surfaces but can be used as input data for simulations of roughness effects using the SPRAY code developed at TU Wien (Cupak et al. 2021). SPRAY is a numerical code that takes data from common BCA codes and AFM images as input and uses a ray-tracing algorithm to calculate sputter yields and angular distributions of sputtered atoms for rough surfaces.

Regarding the BCA simulations, previous work by Szabo et al. described a set of input parameters for SDTrimSP, which were able to reproduce experimental sputter yields for a wide range of ions impinging on pyroxen(oid)es (Szabo et al. 2020a). Furthermore, simulations with these parameters could also be embedded into a self consistent model of potential sputtering, where additional depletion of oxygen from the very surface is assumed. The adaptation consists of increasing the surface binding energy of oxygen bound in the oxides to 6.5 eV, using the surface binding model with parameter $isbv = 2$ and changing the density to match literature values of the minerals. SDTrimSP simulations were performed with those parameters, evaluating sputter yields for the ion/material combinations presented in this study using the graphical user interface (GUI) companion program, which allows for a fast setup of complex simulation settings in SDTrimSP (Szabo et al. 2022b). Figure 5 shows the sputter yield as calculated with SDTrimSP for 2 keV Ar^+ (left) and 4 keV He^+ (right) impacting on atomically flat enstatite ($MgSiO_3$) with a density of $\rho = 3.3$ g cm^{-3} (Bladh et al. 2001). The pronounced increase
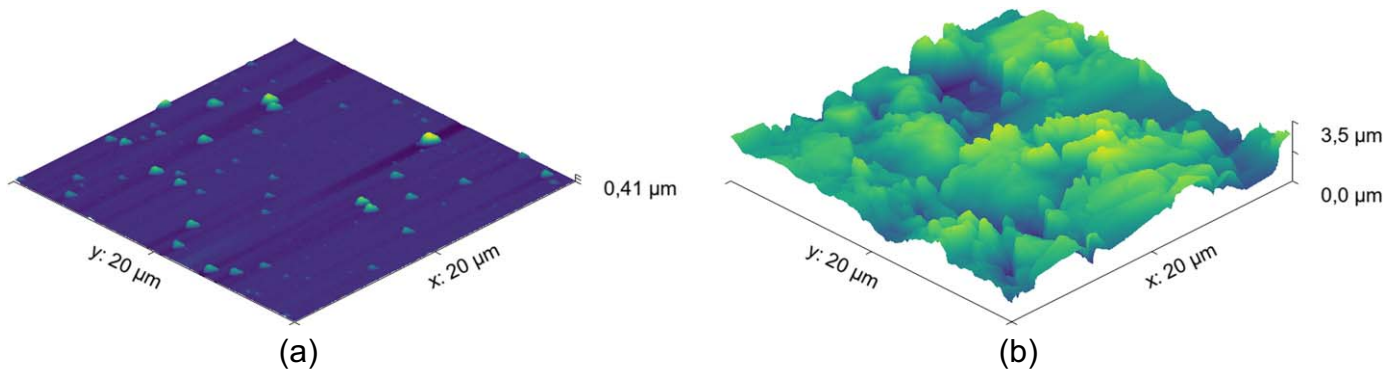
Figure 6. Three-dimensional projections of AFM images of both the enstatite coated QCM (left) and an enstatite pellet (right) before irradiation.
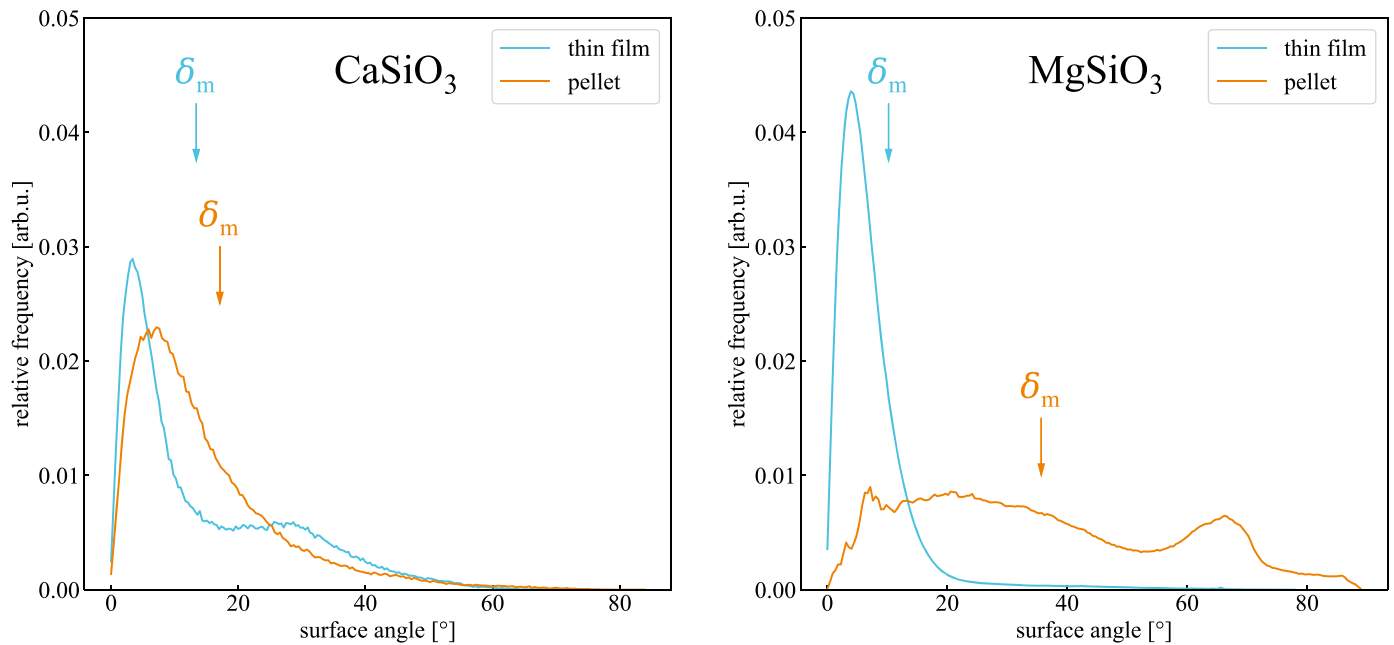

Figure 7. Representative distributions of the local inclinations based on AFM measurements of the irradiated samples. Distributions are shown for both types (thin film on a QCM and pellet) separated by material—wollastonite (left) and enstatite (right). The roughness parameter δ_m for the whole sets of images are indicated with arrows.

Table 3
Roughness Parameter δ_m of the Used Samples Obtained from Sets of AFM Images

	Mean Surface Inclination Angle δ_m	
	Enstatite	Wollastonite
Thin Film	$10.2° \pm 2.1°$	$13.4° \pm 4.4°$
Pellet	$35.7° \pm 4.5°$	$17.1° \pm 2.8°$

of the sputter yield toward larger ion incidence angles for Ar is not fully captured by the simulations, but the overall agreement with the experimental data for the thin film samples is still good, especially when taking the results for He into account. The input sputtering data required for the SPRAY code was also generated with those settings.

To calculate the effect of the rough pellet surfaces, we used the SPRAY code (Cupak et al. 2021) with sets of AFM images obtained from the pellet. It takes several effects into account, including redeposition of ejected material. For redeposition we assumed perfect sticking. For a sticking probability < 1,

particles which hit but do not stick on a neighboring hill will still be scattered in different directions. Their energy and angular distribution will therefore be significantly different from the sputtered particles directly leaving the surface.

The code's main advantages are the drastically reduced computation time compared with 3D BCA codes, as only geometrical information is calculated via a ray-tracing algorithm and the possibility to simulate large areas. The thin film samples have been shown to be fairly flat, with δ_m values of $10.1°$ and $13.4°$ for the wollastonite and the enstatite respectively. Therefore, roughness effects were only simulated for the pellet samples. Table 4 shows results of both SDTrimSP and SPRAY. The ratio between the two is given in the brackets. Sputter yields simulated by SPRAY for the rough pellet surface are compared in Figure 5 to experimental pellet sputter yields.

Regarding the wollastonite pellet, SPRAY only calculates a reduction of 3% for an incidence angle of $\alpha = 45°$ and 16% for $60°$. Considering that the thin films are not perfectly flat either, this agrees well with the experimental results. In the case of enstatite, a more significant reduction of the sputter yield is expected for the pellet due to the pronounced surface roughness

Table 4
Sputter Yields Simulated Using SDTrimSP for Flat Samples and Using the Ray-tracing Code SPRAY with AFM Images as Input for the Rough Samples

	Simulated Sputter Yields [amu/ion]					
α	Wollastonite		Enstatite			
	Ar		Ar		He	
	SDTrimSP	SPRAY	SDTrimSP	SPRAY	SDTrimSP	SPRAY
45°	60.16	58.35 ± 1.11 (0.97)	61.35	43.94 ± 3.56 (0.72)	4.40	4.06 ± 0.22 (0.92)
60°	98.28	82.46 ± 3.77 (0.84)	97.84	55.80 ± 5.38 (0.57)	7.99	5.53 ± 0.65 (0.69)

Note. Brackets indicate the ratio between SPRAY and SDtrimSP.

Table 5
Composition of the Enstatite Thin Film in Atomic Percent, Obtained Using Time-of-flight Elastic Recoil Detection Analysis with an 36 MeV I^{8+} Ion Beam (Moro et al. 2019)

Enstatite Film Composition [at.%]		
	Relative Abundance	Uncertainty—statistics
O	58.2	<0.4
Mg	20.9	<0.4
Si	20.0	<0.4
C	0.5	0.2
Fe	0.3	0.1
H	0.2	0.1

as compared with the thin film. SPRAY simulations also predict such a decrease for all simulated scenarios. For 2 keV Ar^+, the reduction is in almost perfect agreement with the experiments, while there is a slightly larger deviation for 4 keV He^+. Here, SPRAY also predicts a reduction, but less than actually observed. This might be related to the relatively strong increase in sputter yield from SDTrimSP simulations for impact angles of $\alpha > 60°$, peaking at 82° (see solid lines in Figure 5), which has not been verified experimentally yet. With these data as input, facets with increased local impact angles of incidence $\alpha_{loc} > \alpha$ can lead to an increase of predicted sputter yield for a wider range of α_{loc}. Additionally, those facets have a significantly increased sputter yield compared with nominal incidence angles α, even increasing by 390% from $\alpha = 45°$ to $\alpha = 82°$. Another explanation for the remaining small differences could be insufficient sampling of the rough surface by the AFM. Elevations of some 100 nm within a few 10 nm of lateral movement of the AFM tip can lead to smeared out hard edges which are, however, responsible for shadowing effects. Furthermore, the experimental setup allows only to take a slice through the angular distribution of ejecta. Therefore only the polar angle distribution can be probed. Overall, however, we conclude that the differences between pellet and thin film irradiation can very well be explained by surface roughness alone for the given materials. Therefore, amorphous and polycrystalline silicates show the same sputter behavior. This has implications for past experiments—validating the importance of past measurements with silicate based amorphous thin films deposited on QCMs—as well as for interpreting the situation on celestial bodies like Mercury, where a partly amorphized surface is present due to solar wind irradiations and overturning of material (Domingue et al. 2014). However more research should be carried out to confirm that this is a universal finding also applicable for a broader range of materials.

Measurements of the angular distribution of sputtered particles allowed not only to observe the significant impact of surface roughness on the sputter yield, but also a change in the distribution of sputtered particles. Their emission profile is shifted more toward the surface normal compared with the flat samples. Agreement with SDTrimSP is good, although the simulations predict less emission in forward direction. It has to be noted however, that different results are expected for single crystalline samples, where preferred enhanced emission in some directions has been found in Sigmund (2012). Both impacts of surface roughness on the sputter process have to be taken into account for precise modeling of the exosphere on rocky bodies, even more so when considering the presence of porous regolith on its surface. Further experimental and modeling studies should be done to help quantify this effect for a regolith-covered surface.

5. Summary and Conclusion

We have developed a new technique to determine sputter yields of real mineral samples in the form of pressed powder as analogs for the surfaces of rocky planets like Mercury. The method allows to measure the angular distribution of sputtered particles. By calibration of the measurements with data from thin film samples on quartz crystal microbalances, a successful determination of total sputter yields for pressed mineral pellets was possible. For the Mercury analog material enstatite ($MgSiO_3$) the pellet samples exhibit a significantly reduced sputter yield as compared with an amorphous thin enstatite film produced by PLD. AFM investigations of both surfaces reveal a much higher roughness for the pellet sample. Simulations with the ray-tracing code SPRAY show that this reduction can solely be explained by sputtering on local slopes, shadowing and redeposition effects known for rough surfaces. This is supported by measurements on a flat wollastonite pellet ($CaSiO_3$) that has a similar roughness as the thin films and does not show a reduction in sputter yield. From this we conclude that the often used amorphous thin films are well suited for investigating sputtering of planetary analog materials. The effects of surface roughness on the micrometer-scale, however, are present for realistic surfaces as they are encountered on rocky bodies in space. Therefore, altered sputter yields as well as changes in the angular distribution of sputtered particles need to be taken into account to accurately model space weathering processes and the formation of exospheres. Without additional effects caused by the crystalline phases, simulations and experiments working with amorphous samples as used in this study are well suited for this important task. This outcome is not only of importance for the planet Mercury, but has implications for rocky bodies in general, where the interaction with solar wind ions has to be considered.

Appendix
Sample Composition

A1. Evaluation of Quartz Signals

The sputter yield is typically defined as number of emitted particles per impinging ion. This is problematic when dealing with composite samples, as it can than only be an average over the sputter yields of the singe constituents. Furthermore, sputter yields are typically calculated from mass loss of samples by means of (micro) balances. We therefore define the sputter yield as mass loss per impinging ion as in Equation (A2) with mass change Δm, atomic mass m_u and the number of impinging ions N_{ion}. Combining Sauerbrey's Equation (Sauerbrey 1959) with the assumption of a constant ion current density j impinging across the whole quartz surface A_Q, a mass change per ion and solid angle $Y_{C,\Omega}\left[\frac{amu}{ion\ sr}\right]$ can be calculated:

$$\Delta m = -m_Q \frac{\Delta f}{f_Q} \tag{A1}$$

$$y\left[\frac{amu}{ion}\right] = -\frac{\Delta m/m_u}{N_{ion}} \tag{A2}$$

$$N_{ion} = \frac{I\Delta t}{qe_0} \tag{A3}$$

$$Y_{C,\Omega}\left[\frac{amu}{ion\ sr}\right] = \frac{\Delta m/m_u}{N_{ion}}\frac{1}{\Omega_C} = -\frac{qe_0}{m_u I}\frac{m_Q}{f_Q}\frac{\Delta f}{\Delta t}\frac{1}{\Omega_C}$$
$$\approx -\frac{qe_0}{m_u I}\frac{\rho_Q\,d_Q\,r_C^2}{f_Q}\frac{\Delta f}{\Delta t} \tag{A4}$$

Here, the quartz properties mass (m_Q), resonance frequency (f_Q), thickness (d_Q) and density (ρ_Q), the elementary charge e_0, the total ion current I and changes of mass (Δm) and frequency (Δf) in a time span Δt are used. Assuming the diameter of the quartz's sensitive area A_Q of 38.5 mm^2 as defined in Berger et al. (2017), the solid angle of the catcher at a distance of $r_C = 17$mm results in $\Omega_C \approx 0.13$ sr.
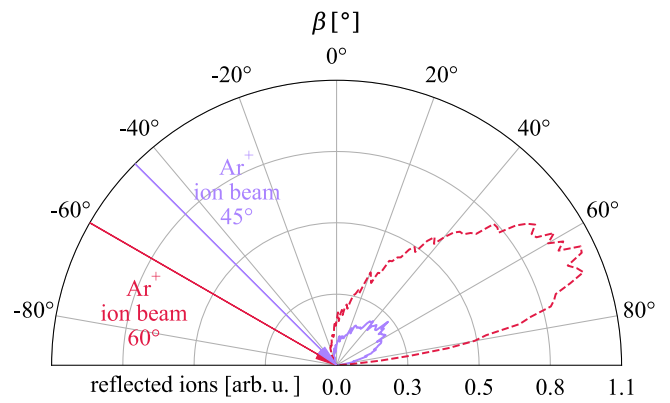

Figure 8. Distributions of reflected ions for 2 keV Ar$^+$ ions impinging on wollastonite (CaSiO$_3$) according to SDTrimSP simulations, restricted to the catcher solid angle. The two incidence angles $\alpha = 45°$ (full purple line) and $\alpha = 60°$ (red dashed line) are compared quantitatively.

A2. Signal Ratio for Wollastonite Irradiations

The signal ratio r for the measurements using wollastonite was calculated from the ratio of a signal weighted sum. This is equivalent to a discrete integration over the data with constant distance in angular spacing:

$$r = \frac{1}{\sum Y_{c,QCM,i}}\sum Y_{c,QCM,i}\frac{Y_{c,Pellet,i}}{Y_{c,QCM,i}} = \frac{\sum Y_{c,Pellet,i}}{\sum Y_{c,QCM,i}} \tag{A5}$$

A3. Reflection of Ions at Flat Surfaces

The reflection of 2 keV Ar$^+$ ions onto wollastonite was calculated with SDTrimSP to show the effect of sputtering of the catcher in forward direction. The experimentally investigated cases of $\alpha = 45°$ and $\alpha = 60°$ are considered, showing different shape and magnitude of the distribution of reflected ions. This is shown in Figure 8.

ORCID iDs

H. Biber ⓘ https://orcid.org/0000-0002-9854-2056
N. Jäggi ⓘ https://orcid.org/0000-0002-2740-7965
A. Galli ⓘ https://orcid.org/0000-0003-2425-3793
P. Wurz ⓘ https://orcid.org/0000-0002-2603-1169
F. Aumayr ⓘ https://orcid.org/0000-0002-9788-0934

References

Arredondo, R., Oberkofler, M., Schwarz-Selinger, T., et al. 2019, Nuclear Materials and Energy, 18, 72
Benkhoff, J., van Casteren, J., Hayakawa, H., et al. 2010, P&SS, 58, 2,
Berger, B. M., Szabo, P. S., Stadlmayr, R., & Aumayr, F. 2017, NIMPB, 406, 533
Betz, G., & Wien, K. 1994, IJMSI, 140, 1
Biber, H., Szabo, P. S., Jaggi, N., et al. 2020, NIMPB, 480, 10
Biersack, J. P., & Haggmark, L. G. 1980, NucIM, 174, 257
Bladh, K., Bideaux, R., Anthony-Morton, E., & Nichols, B. 2001, Handbook of Mineralogy (Berkeley, CA: Mineralogical Society of America)
Carrez, P., Demyk, K., Cordier, P., et al. 2002, M&PS, 37, 1599
Coe, R. S., & Paterson, M. S. 1969, JGR, 74, 4921
Cupak, C., Szabo, P. S., Biber, H., et al. 2021, ApSS, 570, 151204
Domingue, D. L., Chapman, C. R., Killen, R. M., et al. 2014, SSRv, 181, 121
Eckstein, W., & Preuss, R. 2003, JNuM, 320, 209
Galutschek, E., Trassl, R., Salzborn, E., Aumayr, F., & Winter, H. 2007, JPhCS, 58, 395
Golczewski, A., Dobes, K., Wachter, G., Schmid, M., & Aumayr, F. 2009, NIMPB, 267, 695
Hapke, B. 2001, JGR, 106, 10039

Hayderer, G., Schmid, M., Varga, P., Winter, H. P., & Aumayr, F. 1999, RScI, 70, 3696

Hijazi, H., Bannister, M. E., Meyer, H. M., Rouleau, C. M., & Meyer, F. W. 2017, JGRE, 122, 1597

Jäggi, N., Galli, A., Wurz, P., et al. 2021, Icar, 365, 114492

Küstner, M., Eckstein, W., Dose, V., & Roth, J. 1998, NIMPB, 145, 320

Küstner, M., Eckstein, W., Hechtl, E., & Roth, J. 1999, JNuM, 265, 22

Loeffler, M. J., Dukes, C. A., & Baragiola, R. A. 2009, JGRE, 114, E03003

McCoy, T. J., Peplowski, P. N., McCubbin, F. M., & Weider, S. Z. 2018, in Mercury: The View after MESSENGER, ed. S. Solomon, L. R. Nittler, & B. J. Anderson (Cambridge: Cambridge Univ. Press), 176

Moro, M. V., Holenak, R., Zendejas Medina, L., Jansson, U., & Primetzhofer, D. 2019, TSF, 686, 137416

Morrissey, L. S., Tucker, O. J., Killen, R. M., Nakhla, S., & Savin, D. W. 2022, ApJL, 925, L6

Mutzke, A., Schneider, R., Eckstein, W., et al. 2019, IPP Report 2019-02

Sauerbrey, G. 1959, ZPhy, 155, 206

Schaible, M. J., Dukes, C. A., Hutcherson, A. C., et al. 2017, JGRE, 122, 1968

Schlueter, K., Nordlund, K., Hobler, G., et al. 2020, PhRvL, 125, 225502

Sigmund, P. 2012, TSF, 520, 6031

Stadlmayr, R., Szabo, P. S., Biber, H., et al. 2020a, RScI, 91, 125104

Stadlmayr, R., Szabo, P. S., Mayer, D., et al. 2020b, JNuM, 532, 152019

Szabo, P. S., Biber, H., Jäggi, N., et al. 2020b, JGRE, 125, e06583

Szabo, P. S., Biber, H., Jäggi, N., et al. 2020a, ApJ, 891, 100

Szabo, P. S., Chiba, R., Biber, H., et al. 2018, Icar, 314, 98

Szabo, P. S., Cupak, C., Biber, H., et al. 2022a, Surfaces and Interfaces, 30, 101924

Szabo, P. S., Weichselbaum, D., Biber, H., et al. 2022b, NIMPB, 522, 47

Wurz, P., Fatemi, S., Galli, A., et al. 2022, SSRv, 218, 1

Wurz, P., Whitby, J. A., Rohner, U., et al. 2010, P&SS, 58, 1599

Zhu, C., Crandall, P. B., Gillis-Davis, J. J., et al. 2019, PNAS, 116, 11165